Development of nanostructured lanthanum strontium cobalt ferrite/gadolinian-doped ceria composite electrodes of solid oxide cells formed by in situ polarization

Yi Sun,[1,2] Shuai He,[3] Zhishan Li,[1] Abbie C. Mclaughlin,[4] Kongfa Chen,[5] Zongping Shao,[2,*] San Ping Jiang[1,*]

[1]*National Energy Key Laboratory for New Hydrogen-Ammonia Energy Technologies, Foshan Xianhu Laboratory, Foshan 528216, China*;

[2]*WA School of Mines: Minerals, Energy and Chemical Engineering, Curtin University, WA 6102, Australia*;

[3]*Petrochemical Research Institute, PetroChina Company Limited, Beijing 102206, China*;

[4]*Department of Chemistry, University of Aberdeen, Meston Walk, Aberdeen, AB24 3UE, UK*;

[5]*College of Materials Science and Engineering, Fuzhou University, Fuzhou, Fujian 350108, China*;

Corresponding author: Email: zongping.shao@curtin.edu.au (Zongping Shao); s.jiang@curtin.edu.au (San Ping Jiang)

ABSTRACT

In the development of nano-scale oxygen electrodes of the high temperature solid oxide cells (SOCs), the interface formed between the nanoelectrode particles and the electrolyte or electrolyte scaffolds is most critical. In this work, a new synthesis technique for the fabrication of nano-structured electrodes via *in situ* electrochemical polarisation treatment is reported. Lanthanum strontium cobalt ferrite (LSCF) precursor solution is infiltrated into gadolinia-doped ceria (GDC) scaffold pre-sintered on yttria-stabilized zirconia (YSZ) electrolyte, followed by *in situ* polarisation current treatment at SOC operation temperatures. Electrode ohmic and polarisation resistances decrease with the increase of polarisation current treatment. Detailed microstructure analysis indicates the formation of convex-shaped interface between LSCF nanoparticles (NPs) and GDC scaffold, very different from flat contact between LSCF and GDC observed after heated at 800ºC with no polarization current treatment. The embedded LSCF NPs on GDC scaffold contribute to the superior stability under both fuel cell and electrolysis operation conditions at 750ºC, and a high peak power density of 1.58 Wcm^{-2} at 750°C. This work highlights a novel and facile route to *in-situ* construct stable and high-performing nanostructured electrode for SOCs.

KEYWORDS: solid oxide cells, nano-structured LSCF/GDC composite electrodes, in situ polarization treatment, convex-shaped interface, embedded LSCF nanoparticles, stable electrode nanostructure.

1. INTRODUCTION

The solid oxide cell (SOC) is the most efficient electrochemical energy conversion and storage device, which can be operated reversibly under solid oxide electrolyser cell (SOEC) mode to store renewable electricity from solar and wind in the form of hydrogen fuel and under solid oxide fuel cell (SOFC) mode to generate electricity by consuming the generated hydrogen[1-6]. Conventional SOCs consisted of oxide ion conducting electrolytes such as yttria-stabilized zirconia (YSZ) sandwiched between of Ni/YSZ cermet fuel electrodes and oxygen electrode such as lanthanum strontium manganite (LSM) usually require operating temperatures in the range of 800-1000°C[4, 7]. Such high operation temperature is not favourable for the long-term stability due to interface delamination and considerable microstructure degradation.[4, 8-9] The most effective strategy to increase the durability of SOCs is to lower the operating temperature to intermediate temperatures of 600-800°C[7, 10-11]. With the reduction in SOC operation temperatures, conventional electrode materials in particular oxygen electrodes such as LSM are no longer applicable due to the increasingly dominated polarization loss for the oxygen reduction and oxygen evolution reactions (ORR and OER) owing to the high activation energy and low ionic conductivity of the materials[12-16]. This leads to the significant development in the mixed ionic and electronic conducting (MIEC) materials such as lanthanum strontium cobalt ferrite (LSCF)[15] and barium strontium cobalt ferrite (BSCF)[17-18] as oxygen electrodes to substantially reduce the polarisation resistance due to the extended three phase boundaries (TPB)[19]. However, cobaltite-based perovskites react readily with YSZ electrolytes, which limits the wide application of LSCF and BSCF based electrode materials in YSZ electrolyte based SOCs.

Development of nano-structured electrodes is also very effective to increase the electrode activity at intermittent temperatures such as well-known infiltration and exsolution.[20-21] In the exsolution method, transition or noble metal oxides are doped at the B-site of a parent perovskite lattice in an oxidizing atmosphere, and then exoluted under reducing environment or under cathodic polarization, forming nanosized metallic particles on the surface of host electrodes[19, 22-23]. Such exsoluted nanoparticles (NPs) not only improve the electrode

performance but also show the high structural stability against agglomeration. However, this method suffers from several limitations. For example, the number of nanocatalysts generated are far from sufficient because a large amount of the metal ions still remain in the parent lattice due to the slow cation diffusion rate and excessive reduction may result in the collapse of the electrode structure.[24] Moreover, because of the reducibility requirement in exsolution, the method is limited to a small range of metal oxides which can be applied.[25] Most critically, it is difficult to be applied on the air electrodes as the in situ exsolution generally occurs under reducing conditions[26].

In comparison, the impregnation or infiltration method is a versatile technique to form electrochemically active NPs for both fuel and air electrodes.[27-29] In this method, a porous scaffold supported by an electrolyte is employed, followed by infiltration or impregnation of a precursor solution with active elements and components for the electrode reactions and heat-treated at relatively low temperatures to form uniformly distributed NPs on the surface of scaffolds[30]. A MIEC scaffold or more than one active components can be used in this method.[31-33] The main issue for the infiltration technique is that agglomeration of NPs occurs under SOC operating temperatures probably due to the poor interface between the infiltrated NPs and surface of the supported scaffolds. For example, Shah et al investigated the impact of firing temperature of LSCF infiltrating on GDC scaffold on the polarization resistance and showed an increase of electrode polarization resistance when temperature increases from 800 °C to 1200°C due to the growth of LSCF particle size, from 50 nm to 1 μm.[34] Further studies on the time-dependent performance of LSCF infiltrated GDC cathode found that the LSCF nanoparticle size doubled after aging at 800°C in air for 200h, while the electrode polarization resistance, R_p also increased from 0.2 to 0.43 Ωcm^2.[35] Without the high temperature treatment, a strong interface bond between the infiltrated nanoparticles and supported electrode is difficult to establish resulting in the phase migration and deterioration in the electrode activity during the operation. The infiltration method also suffers from the requirement of multiple infiltration and sintering steps, which increase the complex and cost of cell fabrication. Excess infiltration would also reduce the porosity and block the pathway for gas diffusion.

To avoid the limitations of both exsolution and infiltration techniques, our group developed a directly assembly process without the need of high-temperature electrode calcination process. In this method, electrode ink or paste is directly applied to the electrolyte surface and the electrode/electrolyte interface is induced via the in-situ application of cathodic polarization current at the SOC operating temperatures. The method has been proven effective on

conventional screen printed LSM and LSCF air electrodes on YSZ and GDC electrolytes, and Ni based fuel electrodes, showing high activity and excellent stability under both cathodic and anodic polarization conditions[36-40]. The method is further combined with the decoration method for the development of high-performance composite electrodes[26, 41]. However, under prolonged operation under SOC conditions, microstructure change and agglomeration of the decorated phase also takes place due to the relatively weak interface between the decorated NPs and the electrolyte. The interface formed between the electrode/electrolyte and the one between the NPs within the electrodes are both critical for the performance and durability of the nano-scaled electrodes of SOCs.[20, 42]

To take the advantage of both infiltration and direct assembly techniques, we developed an innovative way to fabricate nano-structured electrodes supported on porous scaffolds with high activity and high structural stability of the formed nano-scaled electrodes. In this new method, ionic conducting scaffold is first pre-sintered on YSZ electrolyte, forming strong interface between the scaffold and the electrolyte. Precursor solution with active elements is infiltrated into pre-sintered scaffold, followed by in situ polarization current treatment. Upon application of a polarisation current, phase formation and strong bonding/interface between the infiltrated NPs and scaffold occur simultaneously. The interface between the infiltrated NPs and electrode supports is characterized by the convex-shaped contact marks, which in turn inhibit the agglomeration of infiltrated NPs and thus achieve high and stable performance. The method is schematically shown in **Fig.1**. To demonstrate the feasibility of the technique, LSCF nitrate precursor solution was infiltrated into GDC scaffold pre-sintered on YSZ electrolyte, followed by cathodic polarization treatment at 700°C, 750°C and 800°C. The results clearly show the convex interface formation between the infiltrated LSCF NPs and GDC scaffold and excellent electrochemical performance and stability of as-prepared LSCF/GDC composite electrodes under SOC operation conditions.

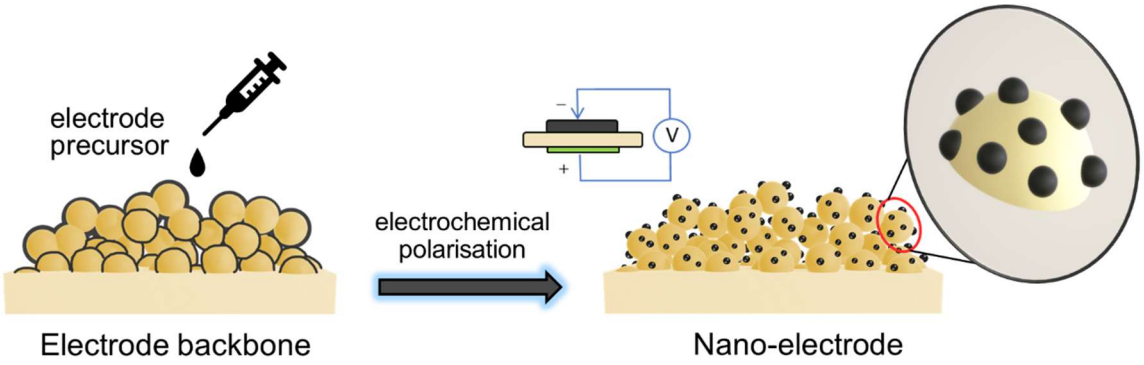

Figure 1. Scheme of in situ polarization induced nano-structured electrodes on GDC scaffold pre-sintered on YSZ electrolyte. The inset shows the formation of infiltrated nanoparticles embbed on the GDC scaffold by the in situ polarization current treatment.

2. EXPERIMENTAL SECTION

2.1. Preparation of electrolyte and direct assembled cells. The electrolyte pellets with 18 mm diameter and 1 mm thickness were fabricated by die pressing of 8 mol% Y_2O_3 stabilized zirconia powder (YSZ, Tosoh, Japan) and sintered at 1450°C for 5 h. Pt paste (Gwent Electronic Materials Ltd. UK) was printed on the centre and the edge of YSZ pellets as the counter and reference electrodes, respectively and calcined at 1100°C for 2 h. The gap between the counter and reference electrodes was ~ 4 mm. $Gd_{0.1}Ce_{0.9}O_{2-\delta}$ (GDC) scaffold paste was made of $Gd_{0.1}Ce_{0.9}O_{2-\delta}$ powder (AGC Seimi Chemical Co Ltd) and starch mixed by ball mill with weigh ratio 4:1 following by mixing with ink vehicle (Fuel Cell Materials, US). Scaffold paste was printed on the other side of pellets, positioned opposite to counter electrode and then calcined at 1200°C for 2 hrs. The thickness of GDC scaffold was 50-60 μm and the area of scaffold was 0.5 cm^2.

$La_{0.6}Sr_{0.4}Co_{0.2}Fe_{0.8}O_{3-\delta}$ (LSCF or LSCF6428) cathode solution with 0.4 mol/L concentration was made of $La(NO_3)_3 \cdot 6H_2O$ (99.9%, Alfa Aesar, UK), $Sr(NO_3)_2$ (99%, Acros Organics, Australia), $Co(NO_3)_2 \cdot 6H_2O$ (98.0%, Alfa Aesar, UK), $Fe(NO_3)_3 \cdot 9H_2O$ (98.0%, Alfa Aesar, UK) and urea. The ratio of metal ions and urea was 1:1. The precursor solution underwent ultrasonic treatment for 5 min before use. LSCF solution was infiltrated into GDC scaffold and dried at 70°C. Three consecutive infiltration was carried out, following by heating at 450 °C for 10 min. The loading of infiltrated LSCF was 3.00±0.04 mg cm^{-2}, calculated by the weight differences before and after the heat treatment. Pt mesh was used for current collection. LSCF

cathode precursor solutions were calcined at 700°C, 800°C and 900°C for 2h to investigate the phase formation.

Ni/YSZ anode-supported YSZ electrolyte cells (φ 15 mm × 0.8 mm) were prepared by spin-coating method, followed by co-sintering at 1450 °C for 5 h. For the anode support, NiO (Fuel Cells Materials, US), YSZ powder, and tapioca were blended with a weight ratio of 5:5:2.5. The anode functional layer (AFL) was fabricated by mixing YSZ and NiO with a weight ratio of 5:5. GDC scaffold and LSCF infiltration steps on the Ni/YSZ anode-supported YSZ electrolyte cells were the same as that for the half cells. Ag paste (Gwent Electronic Materials Ltd., U.K.) was painted on the electrode surface and dried at 150°C, serving as the current collector. The cathode had a geometric area of 0.5 cm^2 testing at 750°C before and after polarization current treatment at 025-0.5 Acm^{-2} in 97% H_2/3% H_2O and air.

2.2. Characterization. Phase formation of LSCF calcined at different temperatures and compatibility of LSCF between GDC and YSZ was examined by Bruker D8 Advance X-ray diffractometer. The polarization performance for half-cell was measured at 750°C and current density range of 0.2-1.0 Acm^{-2} in open air, and the electrochemical impedance was measured under open circuit conditions in the frequency range from 0.1 Hz to 100 KHz with signal amplitude of 10 mV by a Gamry reference 3000 Potentiostat. Ohmic resistance (R_Ω) was obtained from the high frequency intercept and electrode polarization resistance (R_P) was obtained by the difference between the high and low frequency intercepts. Activation energy was calculated by R_P measured at different temperature range from 600-800°C. To evaluate the cell stability, cell voltage was recorded at cathodic and anodic polarization of 500 mA cm^{-2} at 750°C and 800°C for 50 h, respectively.

Ni/YSZ anode supported YSZ electrolyte cells were sealed onto Al_2O_3 tubes by ceramic bond (Ceramabond 552, Aremco Products Inc.). H_2 at a flow rate of 50 mL min^{-1} was supplied to the NiO/YSZ anode, and the cathode was exposed to the air. The NiO/YSZ anode was reduced in H_2 at 750 °C for 1 h before the electrochemical tests. The polarization performance for the as-prepared cell was measured at 750°C before and after polarization treatment at 0.25 Acm^{-2} and 0.5 Acm^{-2} for 1 h.

The microstructure of LSCF/GDC composite electrodes was acquired by scanning electron microscopy (SEM, Zeiss Neon 40EsB and Tescan Clara FESEM, Czech Republic). LSCF elements distribution around the GDC scaffold and interface between the composite electrode nanoparticle, GDC scaffolds and YSZ electrolyte were investigated by high angle annular dark

field scanning transmission electron microscope (HAADF-STEM, FEI Talos FS200X G2 FEG TEM) after being milled as 70nm lamellae by focused ion beam (FIB Tescan LYRA3 GM). In order to investigate the interfacial contact between LSCF and GDC scaffold, LSCF phase of the composite electrodes was removed by diluted HCl solution treatment.

3. RESULTS AND DISCUSSION

3.1. Phase and Microstructure. Figure 2 shows the XRD pattern of LSCF powder obtained from nitrate precursor solution calcined at 700° C, 800° C and 900° C for 2h in air. LSCF perovskite phase was labelled by diamond symbols and the LSCF perovskite phase intensity increased with the increase of calcined temperature, indicating the formation of the LSCF perovskite phase. However, as shown in the figure, there are small peaks associated with $La(OH)_3$, $La_{0.3}Sr_{1.7}FeO_4$ and $Fe(Co_{1.13}Fe_{0.87})O_4$, showing the presence of minor impurity phases of the precursor solution after the heat treatment. The impurity phase decreases with the increase in the heat treatment temperatures. Nevertheless, the presence of minor cobaltite and ferrite phases in nano-structured electrodes could be beneficial for the promotion of electrocatalytic activity and stability, as recently reported in multiple phased cathodes of SOFCs.[43-44]

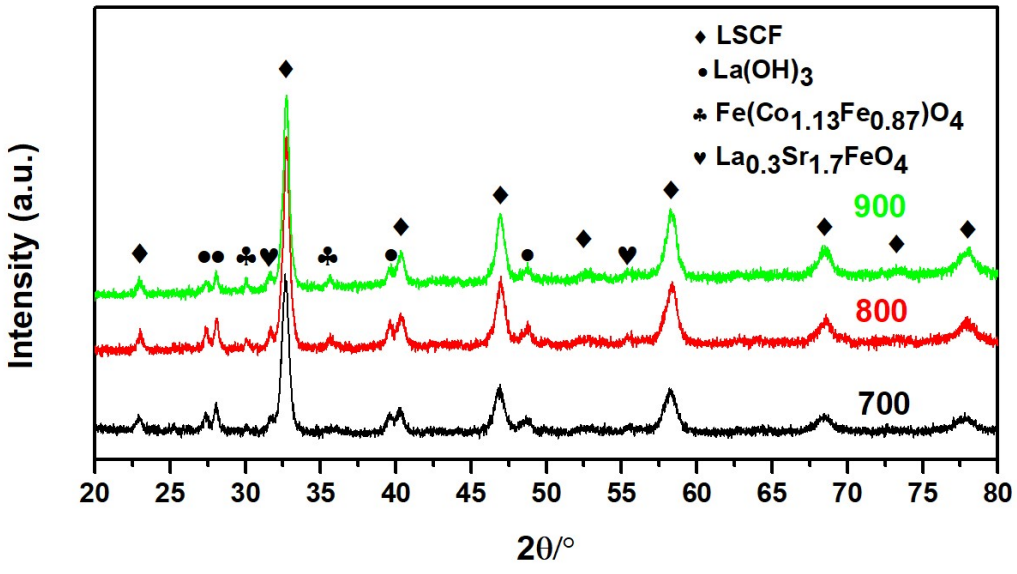

Figure 2. XRD patterns of LSCF cathode powder obtained from precursor solution calcined at 700°C, 800° C and 900° C for 2 h. The numbers in the figure are the calcination temperature of precursor solution.

As showing in the cross section of GDC scaffold on YSZ sintered at 1200°C for 2 h and LSCF infiltrated GDC scaffold sintered at 700°C and 750 °C for 2 h before polarization treatment (**Fig.S1**), the surface of GDC particles is quite smooth and they are well connected with each other (**Fig.S1a**). The GDC particle size was about 200-500 nm and the thickness of the GDC scaffold was ~50 μm with porosity of about 30%. After infiltration of 3 mg cm^{-2} LSCF cathode and sintering at 700°C, LSCF NPs were evenly distributed on the surface of GDC scaffold (**Fig.S1b**). The size of LSCF NPs was in the range of 30 nm. With the increase of the heat-treatment temperature to 800ºC, the size of LSCF nanoparticles grew to ~50 nm. This shows that the NPs formed are sensitive to the heat-treatment temperature.

Figure 3 shows SEM imaging of cross section of LSCF/GDC composite electrodes sintered at 800°C for 2h and polarized under cathodic and anodic polarization at 0.5 A cm^{-2} at 750°C and polarized at 800°C for 100 h. For the LSCF/GDC composite electrodes without polarization current treatment, the surface of GDC scaffold is smooth and the contact marks left by the infiltrated LSCF NPs are difficult to observe (**Fig.3b**). This indicates that the interface formed between infiltrated LSCF NPs and GDC scaffolds is flat and relatively weak (shown schematically in the inset in **Fig.3b**). After cathodic and anodic polarization at 0.5 A cm^{-2} for 50 h at 750°C, there appears to be growth of infiltrated LSCF NPs (**Fig.3c**). Most interesting, after removal of infiltrated LSCF NPs by dilute HCl acid treatment, there was clearly formation of convex-shaped contact marks on the GDC scaffold surface (see the inset circles of **Fig.3d**). The observation of convex-shaped contact marks indicates the formation of intimate and strong interfaces between the infiltrated LSCF NPs and GDC scaffold most likely own to the in situ polarization current treatment. This is the first direct evidence that polarization current treatment not only induces the formation of strong interface between the directly assembled electrode and YSZ (or GDC) electrolyte,[39] but also induces the formation of a convex-shaped interface between the infiltrated LSCF NPs and supported GDC scaffolds within the composite electrode. Further increase in the heat-treatment temperatures to 800 ºC not only increases the size of LSCF NPs but also increases the depth and areas of the convex-shaped interface between the infiltrated LSCF NPs and GDC scaffolds (see **Fig.3f**). The fractured particles as shown in **Fig.3f** show the increased bonding between the GDC particles of the scaffolds.

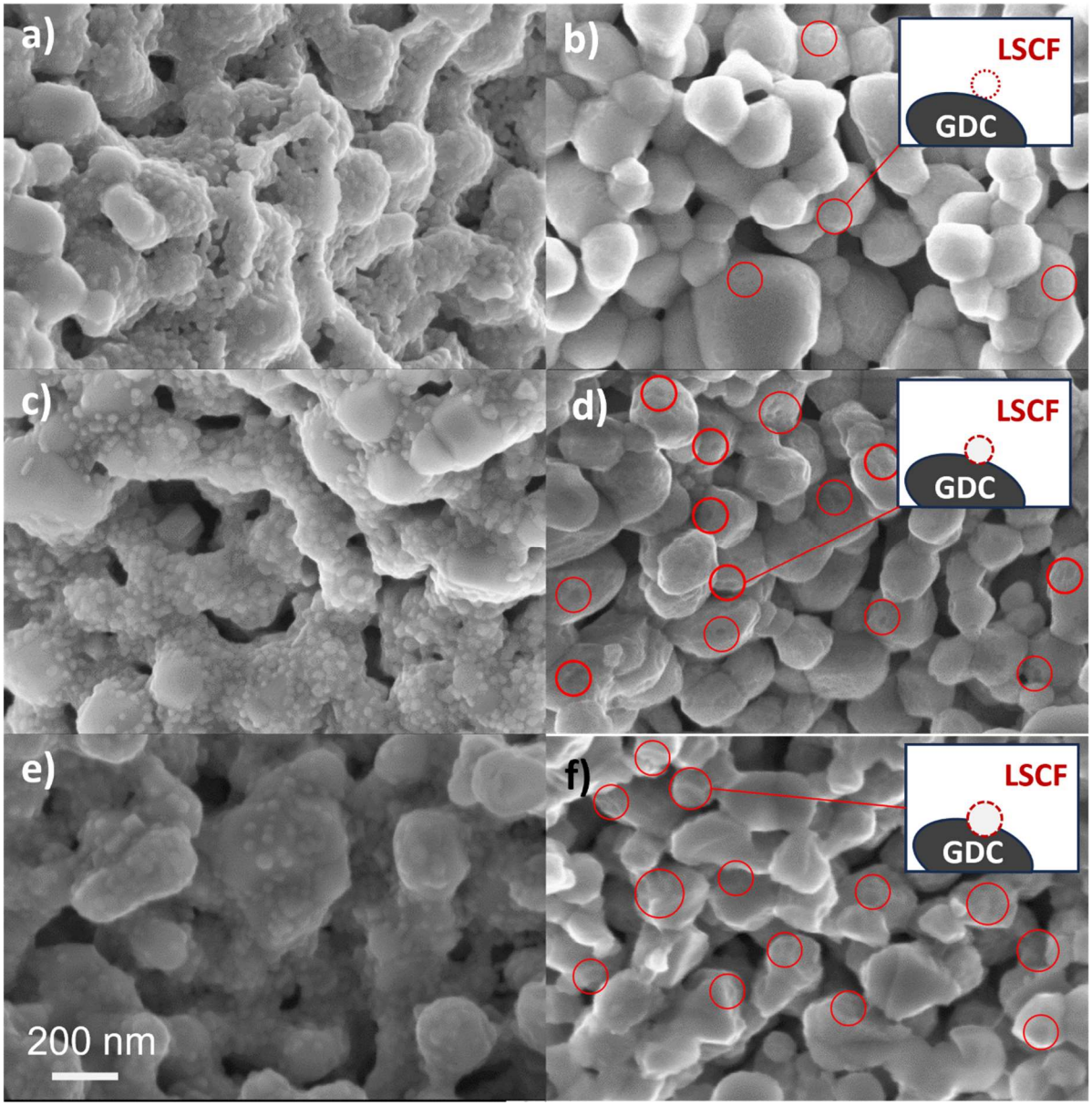

Figure 3. SEM imaging of cross section of LSCF/GDC composite electrodes sintered at (a,b) 800°C for 2h without polarization treatment, (c,d) after cathodic and anodic polarization at 0.5 A cm^{-2} for 50h under each condition at 750°C and (e,f) after cathodic and anodic polarization at 0.5 A cm^{-2} for 50h under each condition at 800°C. In (b)(d)(f) SEM images were taken after the LSCF phase of the composite electrodes was removed by diluted HCl solution treatment. The scale bar in (e) is 200 nm and applies to all figures.

The possible reaction between YSZ electrolyte and LSCF/GDC composite electrode was studied by STEM-EDS mapping (**Fig.S2**). In the figure, Line 1 was drawn through the interface of GDC scaffold and YSZ electrolyte and Line 2 was drawn through the electrode and YSZ electrolyte interface with no GDC scaffold. In the case of the electrodes after cathodic and

anodic polarization at 0.5 A cm^{-2} and 750°C or 800ºC for 50 h, the line scan across the interface between GDC scaffold and YSZ electrolyte shows the presence of Zr and Ce with no detection of Sr (Line 1, **Fig.S2a, b**) as expected. The same was also observed for the open space region at the GDC scaffold and YSZ interface for the electrodes after cathodic and anodic polarization at 0.5 A cm^{-2} and 750°C for 50 h (**Fig.S2a**). This indicates no Sr segregation from the infiltrated LSCF NPs to the YSZ interface. However, with the increase of the polarization current treatment at a higher temperature of 800ºC, accumulation of Sr at the open interface region of YSZ electrolyte is evident and this is clearly indicated by the high Sr content at the interface region (see Line 2, **Fig.S2b**). The accumulation of Sr content at the YSZ interface region shows the Sr segregation and possible formation of $SrZrO_3$ at the LSCF/GDC composite electrodes and YSZ electrolyte interface for the electrodes formed at 800ºC, most likely due to the direct contact of the infiltrated LSCF phase with the YSZ electrolyte. This is consistent with the reported chemical reactivity between LSCF and YSZ, forming insulating products like $La_2Zr_2O_7$ and $SrZrO_3$ at temperatures as low as 800ºC[45-46]. This result clearly demonstrates that the segregation and reaction of Sr from the infiltrated LSCF phase at the electrode/electrolyte interface occurs at 800 ºC but not at 750 ºC. However, as shown in **Fig.S2**, there is no Sr accumulation within the GDC scaffolds, indicating no Sr segregation between the infiltrated LSCF NPs and GDC scaffolds.

The interface between the infiltrated LSCF NPs and GDC scaffold was further investigated by HRTEM and the corresponding FFT micrograph and results are given in **Figure 4**. For the LSCF/GDC interface after heating at 800°C for 2 h without polarization current treatment, observed along $[011]_{GDC}$ and $[001]_{LSCF}$ zone axis, cubic perovskite structure of LSCF and cubic fluoride structure of GDC were identified with labelled index (**Fig.4a**). According to the FFT, the most obvious lattice relationships is drawn on the figure, which $(200)_{GDC}$ is parallel to the $(100)_{LSCF}$. The interface between infiltrated LSCF NPs and GDC scaffold is clean and flat, consistent with that observed in **Fig.3b**. For the interface of LSCF NPs and GDC scaffold after cathodic polarization for 50h and anodic polarization for 50h at 0.5 A cm^{-2} and at 800 °C, there is an evident formation of convex-shaped contact between LSCF and GDC phase, but no clear interfacial separation between LSCF and GDC (**Fig.4b**), indicating the intimate and intermeshed interface formed between LSCF NPs on the GDC scaffold induced by the in situ polarization current treatment. The HTTEM observation is consistent with the convex-shaped interface formed between LSCF NPs and GDC scaffold as shown by the SEM analysis (**Fig.3**), indicating the formation of embedded LSCF NPs on the GDC scaffold. Nevertheless, the

orientation relationship and the lattice mismatch factor (f) between LSCF and GDC phase can be identified as

$$\theta_{\{010\}LSCF/\{111\}GDC} = 5° \quad (1)$$

$$f = \frac{d_{\{010\}LSCF} - d_{\{111\}}}{d_{\{010\}LSCF}} * 100\% = 2\% \quad (2)$$

where $\theta_{\{200\}LSCF/\{220\}GDC}$ represents the angle between the two planes. This indicates the presence of disorientation at the interface between the LSCF and GDC phases. However, the presence of such disorientation and lattice mismatch at the interface would not inhibit the oxygen ions migration and diffusion between LSCF and GDC phases, as shown previously[37, 40, 47].

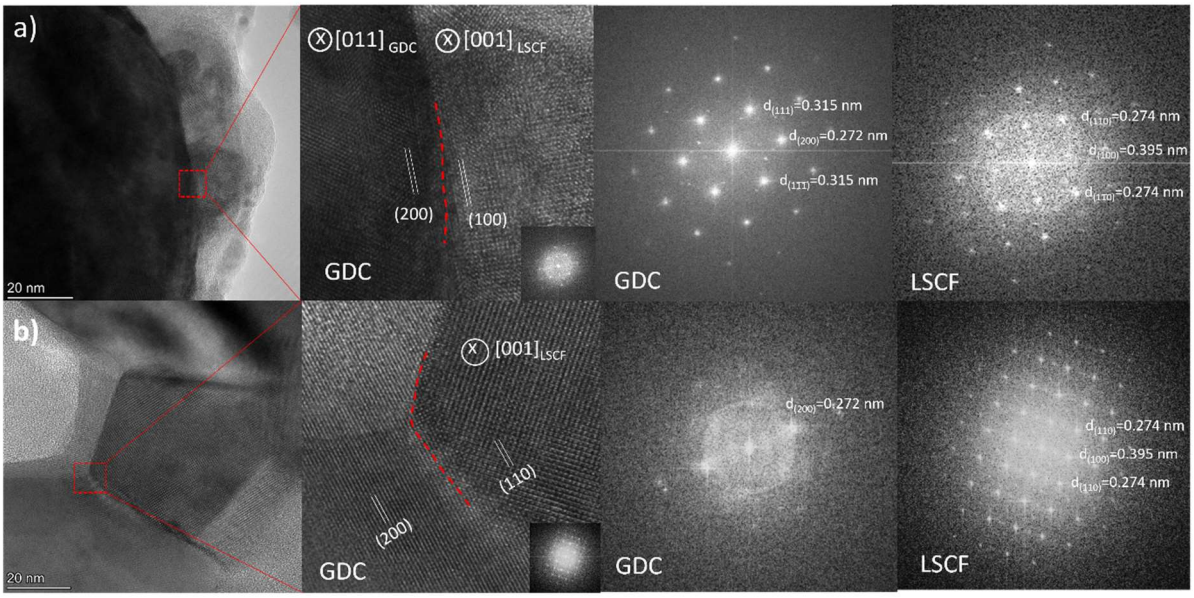

Figure 4 HRTEM and corresponding FFT micrograph of LSCF NPs and GDC scaffold interface (a) after heating at 800°C for 2h with no polarization treatment, observed along $[011]_{GDC}$ and $[001]_{LSCF}$ zone axis, and (b) after in situ cathodic and anodic polarization current treatment at 0.5 A cm^{-2} and 800 °C for 50h, observed along $[001]_{LSCF}$ zone axis.

3.2. Electrochemical Performance. Figure 5 shows the electrochemical performance of the in situ polarisation induced nano-structured LSCF/GDC composite electrode, measured at 700°C as a function of polarisation current density. The composite electrode sample was stayed at the test temperature for 1 h before the electrochemical measurement. The cathode potential, $E_{cathode}$, was measured between the cathode and reference electrode, which include the cathode overpotential and the potential associated with the contact resistance and ohmic resistance of

electrolyte. The high voltage value of $E_{cathode}$ is most likely due to the thick electrolyte discs used. As the electrolyte resistance is assuming constant, the change in $E_{cathode}$ can be considered primarily related to the overpotential change and the change in the contact resistance between the infiltrated LSCF NPs and GDC scaffold. It can be found that the $E_{cathode}$ increases with the increased current density, however, in each cathodic polarisation current, the potential curve is characterised by an initial rapid decrease, followed by a steady state. For example, after applying a polarization current at 1.0 Acm^{-2}, the overall polarization potential decreased from -8.5 V to -5.5 V within 18 mins (**Fig.5a**). Most interesting, the electrode ohmic resistance, R_Ω decreased with the increase of polarisation current treatment. The initial R_Ω was 21.5 Ωcm^2 and reduced substantially to ~11 Ωcm^2 at the end of the test (see **Fig.5b**). The in-situ polarisation treatment also has a significant effect on the electrode polarisation resistance, R_p, which decreases substantially with the increase of the polarisation current. For example, the initial R_p was 6.1 Ω cm^2 and reduced to 1.6 Ω cm^2 after polarization treatment at 1.0 Acm^{-2}. The significant reduction in both R_Ω and R_p is a clear indication of the interface formation between the infiltrated LSCF NPs and GDC scaffold, consistent with previous studies[39, 47]. The electrode impedance behaviour also changes significantly with the applied polarisation treatment. The initial electrode impedance is characterised by three separable impedance arcs. The appearance of three separable impedance arcs may be related to the fact that LSCF phase would not be able to form at such low temperature. With the applied polarization current treatment, the heat generated by the polarization current not only promotes the interface formation between the infiltrated LSCF NPs and GDC scaffold, but also the formation of LSCF phase. This is probably the reason for the change of the three separable impedance arcs to a single and overlapped one. With the application of the polarisation current treatment, the size of the impedance curve is reduced dramatically and the impedance response is characterized by a single and overlapped arc. A single and overlapped arc is an impedance characteristic of the oxygen reduction reaction on LSCF electrodes on GDC electrolyte.[13, 38, 48] This evidently shows the formation of effective LSCF/GDC composite electrodes via the in situ polarization treatment of the infiltrated LSCF in GDC scaffold.

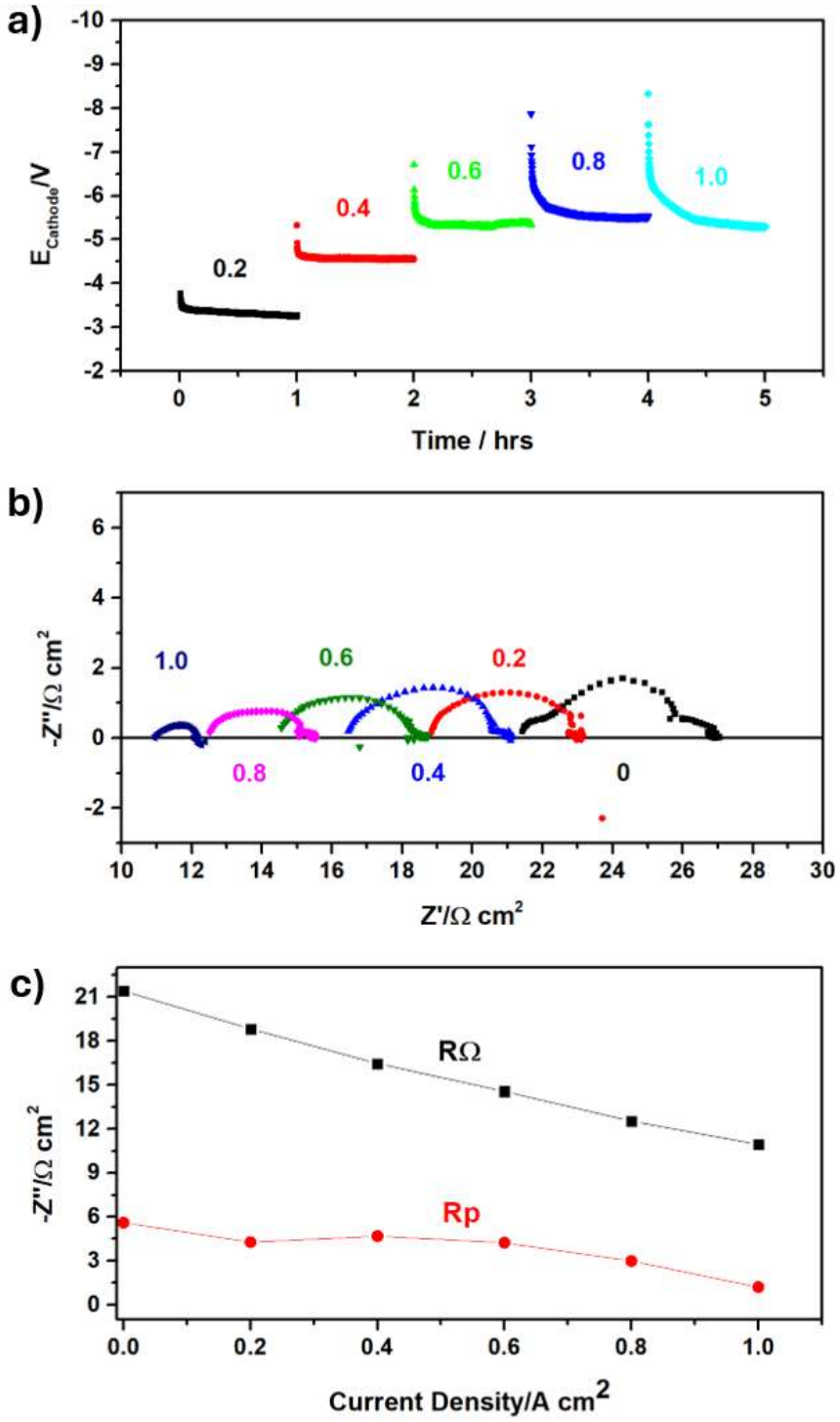

Figure 5 (a) Cathode potential ($E_{cathode}$) of LSCF/GDC composite electrode as a function of polarization time measured at different current density at 700°C, (b) the corresponding electrochemical impedance curves as a function of polarization current treatment and (c) the change of R_Ω and R_P as function of polarization current density. The electrode was in situ polarized at 700 °C and the numbers in the figure are the current density (mA cm^{-2}) used for the polarization treatment.

Similar electrochemical behaviour of the LSCF/GDC composite electrode was also observed for the electrode formed by the in-situ polarization current treatment at 800°C (see **Fig. S3**). The initial impedance response is characterized by a single and overlapped arc at 800°C, rather than three separable impedance arcs as in the case at 700 ºC (**Fig.5b**), an indication of the dominant perovskite phase formation of LSCF after annealing at 800 ºC. Both R_Ω and R_p of the LSCF/GDC composite electrode decrease with increase of polarization current density. Initial value of R_Ω and R_p was 6.1 Ωcm^2 and 0.9 Ωcm^2, respectively. After in situ polarized at 1 Acm^{-2} for 1 h, both R_Ω and R_p was reduced to 3.2 Ωcm^2 and 0.3 Ωcm^2, respectively. The smaller R_Ω and R_p values are most likely due to the increased polarization current treatment temperature of 800°C. For the in situ formed LSCF/GDC composite electrodes, both ohmic and electrode resistances are directly related to the interface formation of the infiltrated LSCF NPs and GDC scaffold because the GDC scaffold was pre-sintered on the YSZ electrolyte. The substantial reduction in both R_Ω and R_p indicates the interface formation between the infiltrated LSCF NPs and GDC scaffold induced by the in situ polarization current treatment. This in turn also indicates that electrochemical active sites of the in situ formed LSCF/GDC composite electrodes are at the LSCF NPs and GDC scaffold and not at the direct contact areas of the infiltrated LSCF NPs and YSZ electrolyte.

Figure 6 shows the electrode impedance curves of the LSCF/GDC composite electrodes measured at different temperatures after the in situ polarization current treatment at 1.0 Acm^{-2} and 700 ºC and 800 ºC and the corresponding activation energy plots. The impedance curves are characterized by an overlapped impedance arc with a significant low frequency inductive loop in the temperature range measured. Chen et al. investigated the relationship between the inductive loop and the size of the infiltrated GDC NPs on LSM scaffold and the results indicated that the low frequency loop disappears when the size of infiltrated GDC NPs increased to around 80 nm after high heat treatment temperature[49]. The presence of nano-sized GDC particles benefit the fast oxygen supply and diffusion for the oxygen reduction reaction. Thus, the appearance of low frequency inductive loop indicates the rapid oxygen reduction reaction at the interface between the embedded LSCF NPs and GDC scaffold[50]. The fast reaction kinetics is also confirmed by the low activation energy values of 67 $kJmol^{-1}$ and 72 $kJmol^{-1}$ for the nano-scaled LSCF/GDC composite electrodes formed by in situ polarization treatment at 700ºC and 800ºC. The activation energy obtained on LSCF/GDC composite

electrodes formed at 700 and 800 ºC is very close, indicating the average activation energy for the O_2 reduction reaction on LSCF/GDC composite electrodes induced by the in situ polarization treatment is ~70 kJmol^{-1}, which is substantially lower than 130-160 kJmol^{-1} reported on pristine LSCF cathodes.[13, 48, 51-52] The reduced activation energy of the nano-scaled LSCF/GDC composite electrodes reported in this work indicates its particular applicability for the intermediate temperature SOCs.

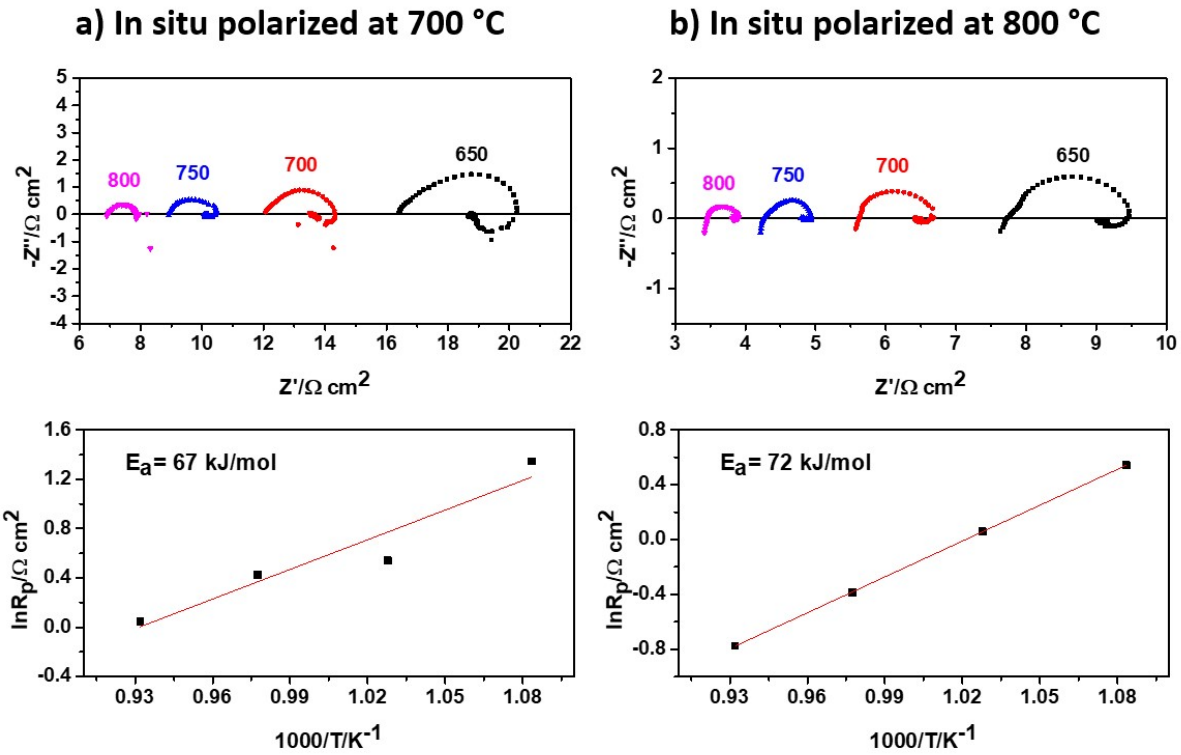

Figure 6 Electrode impedance curves and activation energy plot of the LSCF/DC composite electrodes measured at different temperatures after in situ polarization treatment at 1.0 Acm^{-2} at (a) 700°C and (b) 800ºC. The numbers in the figure are the impedance measurement temperature.

The long-term stability of the LSCF/GDC composite electrodes on YSZ electrolyte under both fuel cell and electrolysis modes was studied at 750°C and the results are shown in **Figure 7**. Operation at 750 ºC can effectively avoid Sr segregation and accumulation at the electrode and YSZ electrolyte interface (see **Fig.S2**), The electrode potential measured between the composite electrode and Pt ring reference electrode, $E_{electrode}$, decreases dramatically in the first 3 h from -3.8 V to -2 V and then reaches a steady state under a cathodic polarization current density of 0.5A cm^{-2} (**Fig.7a**). This indicates the enhanced performance of the LSCF/GDC composite electrodes formed by the in-situ polarization treatment, an indication of the interface

formation between LSCF NPs and GDC scaffold induced by polarization treatment. The enhanced electrode performance is also indicated by the reduction in both R_Ω and R_p (see **Fig.7b**). The rapid increased electrode performance implies that the in situ interface formation of LSCF NPs on GDC scaffold is a very fast and almost instantaneous process. This is very important for the practical application of such in situ nano-scaled electrode fabrication techniques. Switching from cathodic polarization to anodic polarization under the same current density of 0.5A cm^{-2}, the electrode potential increased instantaneously to 2.2 V and then stabilized at 2 V under anodic polarization for 50 h. In the case of anodic polarization, there is a slight increase of ohmic resistance, R_Ω increased from 5.25 Ωcm^2 to 5.63 Ωcm^2 after anodic polarization for 50 h (the total polarization time is 100 h, **Fig.7c**). For anodic polarization, the oxygen electrode undergoes oxygen evolution reaction and during this process, oxygen will be produced at the electrode/electrolyte interface. The formation of oxygen gas builds up the pressure at the interface region, which may cause gradual deterioration of the composite electrode/electrolyte contact. This may be reason for the slight increase of the cell ohmic resistance after anodic polarization for 50 h. However, the increase is very small (i.e., ~0.38 Ωcm^2), indicating that such deterioration effect due to the oxygen evolution is minor. The high stability of the LSCF/GDC composite electrodes on YSZ electrolyte under both fuel cell and electrolysis cell operation modes is most likely due to the strong convex-shaped interface formed between LSCF NPs and GDC scaffold, as shown in **Fig.4**.

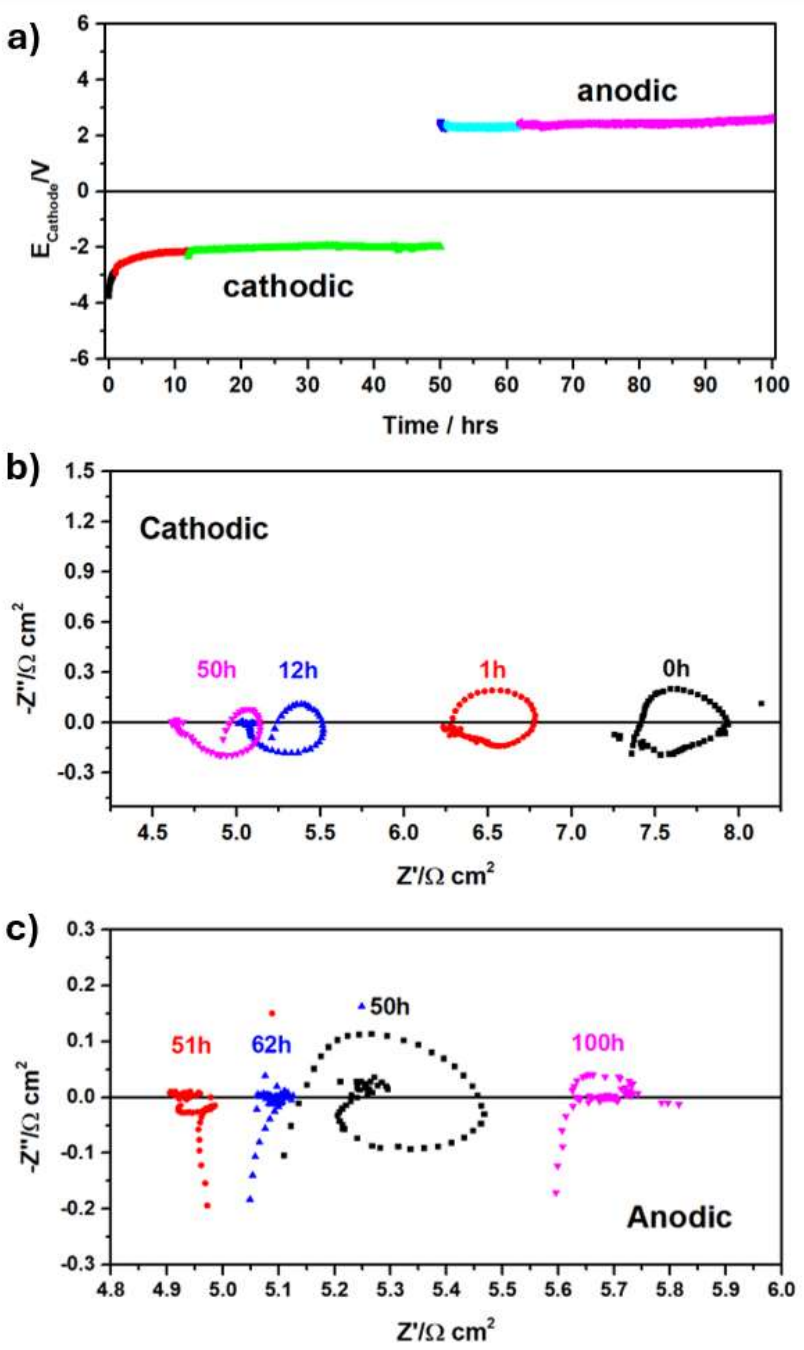

Figure 7 (a) Electrode potential ($E_{electrode}$) of LSCF/GDC composite electrode as a function of polarization time measured at 750°C at 0.5A cm^{-2}, (b) electrochemical impedance curves of the electrode measured under cathodic polarization current and (c) electrochemical impedance curves of the electrode measured under anodic polarization current. Numbers in the figure are the impedance measurement time sequences after the cathodic and anodic polarization treatment.

Figure 8 shows the performance of an as-prepared anode-supported single cell measured at 750°C in H_2-air. The open circuit voltage (OCV) of the as-prepared cell was 1.08 V close to the theoretical value. The as-prepared cell showed an excellent electrochemical performance, reaching a peak powder density (PPD) of 1.58 Wcm^{-2} at 750 °C even before polarization current treatment. The high power output of the as-prepared cell with infiltrated LSCF NPs on GDC scaffold composite cathode is most likely related to the very fast and instantaneous effect of the in situ polarization current on the formation of intimate and convex-shaped interface between infiltrated LSCF NPs and GDC scaffold, as shown above the microstructure and electrochemical activity results. The rapid formation of strong and excellent interface within the composite electrode is also confirmed by the low cell resistance of 0.08 Ω cm^2 and low overall cell polarization resistance of 0.40 Ω cm^2 based on the impedance measurements. Most interesting, after polarization treatment at 0.25 to 0.5 A/cm^2 for 1h, the PPD reduced slightly to 1.4 Wcm^{-2}. The slightly reduced cell performance of the cell after polarization treatment is most likely due to the stabilization of the nano-scaled LSCF/GDC composite electrodes under cell operation conditions. Nevertheless, such change in the electrode microstructure is minor as shown by the similar performance of the cell after polarized at 0.25 Acm^{-2} and 0.5 Acm^{-2} for 1 h.

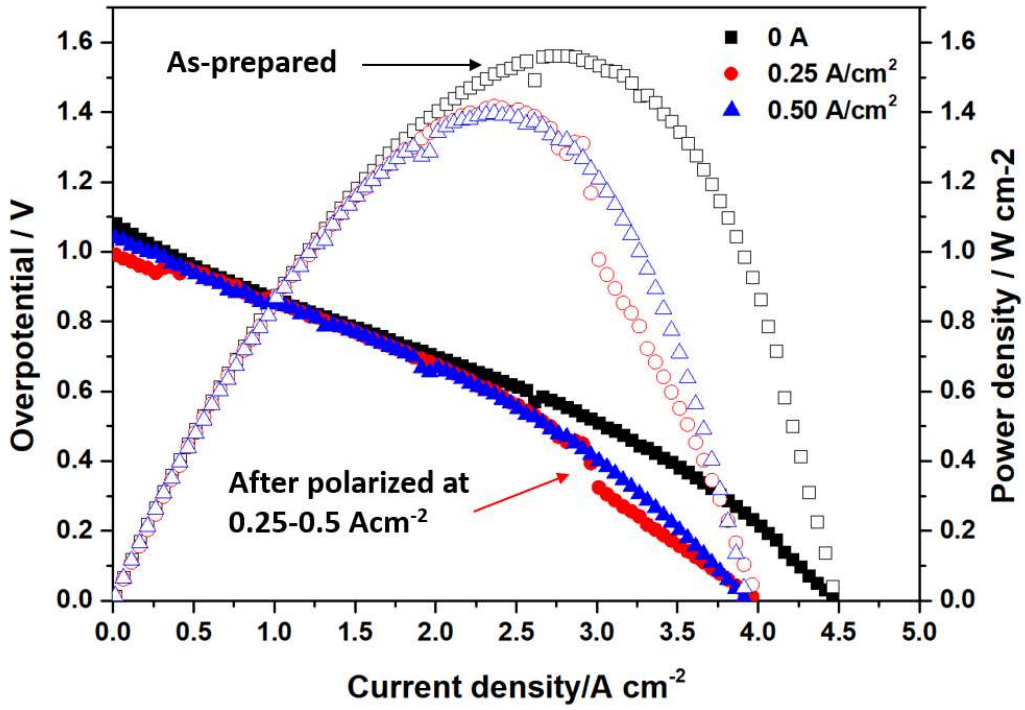

Figure 8 Electrochemical performance of nano-scaled LSCF/GDC composite electrodes on anode-supported YSZ electrolyte cell measured at 750°C of as-prepared cell and the cell after cathodic polarization at 0.25 and 0.5 A cm^{-2} for 1 h.

The stability of LSCF/GDC composite electrodes fabricated by in situ polarization treatment as shown in this study is similar to the Nb-doped $La_{0.6}Sr_{0.4}Co_{0.2}Fe_{0.7}Nb_{0.1}O_{3-\delta}$ (LSCFNb) electrode with 40% $Er_{0.4}Bi_{1.6}O_3$ (ESB) composite electrode fabricated by decoration method and directly assembled on barrier-layer-free YSZ electrolyte.[53] However, activation energy of the LSCF/GDC composite electrodes fabricated by in situ polarization treatment is 70 kJ mol^{-1}, also lower than 98 kJ mol^{-1} reported on LSCFNb/ESB composite electrode with a much high peak power density. The results demonstrate the feasibility of the development of high performance nano-scaled electrodes-based SOCs on barrier-layer-free YSZ electrolyte.

4. CONCLUSIONS

In this paper, we reported a new synthesis method to fabricate nano-structured LSCF/GDC composite electrodes through the interface formation between infiltrated LSCF NPs and GDC scaffold on a YSZ electrolyte via an in situ polarization current treatment. The interface formed between LSCF NPs and GDC scaffold within the composite electrode induced by cathodic polarization current treatment is characterized by the convex-shaped interface, very different from flat interface formed between LSCF NPs and GDC scaffold after heat-treatment but with no polarization current treatment. The convex-shaped interface induced by in situ polarization treatment not only shows high activity for the oxygen reaction with reduced activation energy but also very stable activity for both oxygen reduction and oxygen evolution reactions. This is in contrast with the rather fast microstructure degradation and performance deterioration of infiltrated nano-scaled electrodes formed by simple temperature treatment[27]. The results indicate the most applicable operation temperature for such LSCF/GDC composite electrode on YSZ electrolyte with no GDC protective layer prepared by the reported technique is 750°C. More importantly, this work also demonstrates that the interface formation of LSCF NPs on GDC scaffold through the in situ polarization is a very fast and instantaneous process, evidently confirmed by the high power output of the as-prepared cell (see Fig.8). This present work shows the promising potential of the technique in the practical application in the development of high performance and durable oxygen electrodes of SOCs.

ASSOCIATED CONTENT

Supporting Information

SEM images of GDC scaffold before and after LSCF infiltration, STEM-EDS data of LSCF/GDC electrode after anodic and cathodic polarization, electrochemical data of LSCF/GDC electrode after polarization at 800 °C.

AUTHOR INFORMATION

Corresponding author

San Ping Jiang - *National Energy Key Laboratory for New Hydrogen-Ammonia Energy Technologies, Foshan Xianhu Laboratory, Foshan 528216, China;* and *WA School of Mines: Minerals, Energy and Chemical Engineering, Curtin University, WA 6102, Australia*;

Orcid.org/0000-0002-7042-2976; Email: s.jiang@curtin.edu.au

Zongping Shao - *WA School of Mines: Minerals, Energy and Chemical Engineering, Curtin University, WA 6102, Australia*;

Email: zongping.shao@curtin.edu.au

ACKNOWLEDGMENTS

The project was supported by the Collaborative Doctoral Programme of Curtin-Aberdeen Alliance, Guangdong Basic and Applied Basic Research Foundation (2022A1515110491), and Foshan Xianhu Laboratory Young Fellowship Program (XHQN2022-004).

REFERENCES

1. Chen, K.; Liu, S.-S.; Ai, N.; Koyama, M.; Jiang, S. P., Why Solid Oxide Cells Can Be Reversibly Operated in Solid Oxide Electrolysis Cell and Fuel Cell Modes? *Physical Chemistry Chemical Physics* **2015,** *17*, 31308-31315.
2. Bi, L.; Boulfrad, S.; Traversa, E., Steam Electrolysis by Solid Oxide Electrolysis Cells (Soecs) with Proton-Conducting Oxides. *Chemical Society Reviews* **2014,** *43*, 8255-8270.
3. Gómez, S. Y.; Hotza, D., Current Developments in Reversible Solid Oxide Fuel Cells. *Renewable and Sustainable Energy Reviews* **2016,** *61*, 155-174.
4. Mori, T.; Wepf, R.; Jiang, S. P., Future Prospects for the Design of 'State-of-the-Art' Solid Oxide Fuel Cells. *Journal of Physics-Energy* **2020,** *2*, 031001.
5. Jiang, S. P., Solid-State Electrochemistry and Solid Oxide Fuel Cells: Status and Future Prospects. *Electrochemical Energy Reviews* **2022,** *5*, 21.
6. Yang, Y. P.; Lei, J. Y.; Huang, X. R.; Liao, Z. H.; Liu, Y.; Tu, Z. K., Recent Development in Reversible Solid Oxide Fuel Cells: Theory, Integration and Prospective. *Chemelectrochem* **2023**, e202300593.
7. Wachsman, E.; Ishihara, T.; Kilner, J., Low-Temperature Solid-Oxide Fuel Cells. *MRS Bulletin* **2014,** *39*, 773-779.

8. Wang, H.; Yakal-Kremski, K. J.; Yeh, T.; Rupp, G. M.; Limbeck, A.; Fleig, J.; Barnett, S. A., Mechanisms of Performance Degradation of (La,Sr)(Co,Fe)O3-Δ Solid Oxide Fuel Cell Cathodes. *Journal of The Electrochemical Society* **2016,** *163*, F581-F585.
9. Chen, K.; Jiang, S. P., Review—Materials Degradation of Solid Oxide Electrolysis Cells. *Journal of The Electrochemical Society* **2016,** *163*, F3070-F3083.
10. Wachsman, E. D.; Lee, K. T., Lowering the Temperature of Solid Oxide Fuel Cells. *Science* **2011,** *334*, 935-939.
11. Sun, C.; Hui, R.; Roller, J., Cathode Materials for Solid Oxide Fuel Cells: A Review. *Journal of Solid State Electrochemistry* **2010,** *14*, 1125-1144.
12. Lee, K. T.; Jung, D. W.; Yoon, H. S.; Lidie, A. A.; Camaratta, M. A.; Wachsman, E. D., Interfacial Modification of La0.80sr0.20mno3−Δ–Er0.4bi0.6o3 Cathodes for High Performance Lower Temperature Solid Oxide Fuel Cells. *Journal of Power Sources* **2012,** *220*, 324-330.
13. Jiang, S. P., A Comparison of O-2 Reduction Reactions on Porous (La,Sr)Mno3 and (La,Sr)(Co,Fe)O-3 Electrodes. *Solid State Ionics* **2002,** *146*, 1-22.
14. Jiang, S. P., Development of Lanthanum Strontium Manganite Perovskite Cathode Materials of Solid Oxide Fuel Cells: A Review. *J. Mater. Sci.* **2008,** *43*, 6799-6833.
15. Jiang, S. P., Development of Lanthanum Strontium Cobalt Ferrite Perovskite Electrodes of Solid Oxide Fuel Cells - a Review. *Int. J. Hydrog. Energy* **2019,** *44*, 7448-7493.
16. Yang, G. M.; Su, C.; Shi, H. G.; Zhu, Y. L.; Song, Y. F.; Zhou, W.; Shao, Z. P., Toward Reducing the Operation Temperature of Solid Oxide Fuel Cells: Our Past 15 Years of Efforts in Cathode Development. *Energy Fuels* **2020,** *34*, 15169-15194.
17. Shao, Z.; Haile, S. M., A High-Performance Cathode for the Next Generation of Solid-Oxide Fuel Cells. *Nature* **2004,** *431*, 170-173.
18. Yang, H. R.; Zhong, T.; Chen, Z. Y.; Wang, X.; Ai, N.; Jiang, S. P.; Guan, C. Z.; Fang, H. H.; Luo, Y.; Chen, K. F., Developing an Ultrafine Ba_{0.5}Sr_{0.5}Co_{0.8}Fe_{0.2}O_{3- Δ} Cathode for Efficient Solid Oxide Fuel Cells. *Ceram. Int.* **2022,** *48*, 11419-11427.
19. Irvine, J. T. S.; Neagu, D.; Verbraeken, M. C.; Chatzichristodoulou, C.; Graves, C.; Mogensen, M. B., Evolution of the Electrochemical Interface in High-Temperature Fuel Cells and Electrolysers. *Nature Energy* **2016,** *1*, 15014.
20. He, S.; Zou, Y. F.; Chen, K. F.; Li, N.; Li, D.; Jiang, S. P., A Critical Review of the Nano-Structured Electrodes of Solid Oxide Cells. *Chem. Commun.* **2022,** *58*, 10619-10626.
21. Cao, J. F.; Ji, Y. X.; Shao, Z. P., Nanotechnologies in Ceramic Electrochemical Cells. *Chem. Soc. Rev.* **2024,** *53*, 450-501.
22. Myung, J.-h.; Neagu, D.; Miller, D. N.; Irvine, J. T. S., Switching on Electrocatalytic Activity in Solid Oxide Cells. *Nature* **2016,** *537*, 528-531.
23. Neagu, D.; Oh, T.-S.; Miller, D. N.; Ménard, H.; Bukhari, S. M.; Gamble, S. R.; Gorte, R. J.; Vohs, J. M.; Irvine, J. T. S., Nano-Socketed Nickel Particles with Enhanced Coking Resistance Grown in Situ by Redox Exsolution. *Nature Communications* **2015,** *6*, 8120.
24. Namgung, Y.; Hong, J.; Kumar, A.; Lim, D.-K.; Song, S.-J., One Step Infiltration Induced Multi-Cation Oxide Nanocatalyst for Load Proof Sofc Application. *Applied Catalysis B: Environmental* **2020,** *267*, 118374.
25. Zhu, S. S.; Fan, J. D.; Li, Z. B.; Wu, J.; Xiao, M. Q.; Du, P. X.; Wang, X.; Jia, L. C., Metal Exsolution from Perovskite-Based Anodes in Solid Oxide Fuel Cells. *Chem. Commun.* **2024,** *60*, 1062.
26. Chen, Z.; Jiang, L.; He, S.; Guan, C.; Zou, Y.; Yue, Z.; Ai, N.; Jiang, S. P.; Shao, Y.; Chen, K., Development of Intertwined Nanostructured Multi-Phase Air Electrodes for Efficient and Durable Reversible Solid Oxide Cells. *Applied Catalysis B: Environmental* **2022,** *305*, 121056.
27. Jiang, S. P., Nanoscale and Nano-Structured Electrodes of Solid Oxide Fuel Cells by Infiltration: Advances and Challenges. *International journal of hydrogen energy* **2012,** *37*, 449-470.

28. Liu, Z. B.; Liu, B. B.; Ding, D.; Liu, M. F.; Chen, F. L.; Xia, C. R., Fabrication and Modification of Solid Oxide Fuel Cell Anodes Via Wet Impregnation/Infiltration Technique. *J. Power Sources* **2013,** *237*, 243-259.
29. Guo, S. H.; Li, Y. F.; Han, D. L., Strategy to Improve Electrochemical Performance and Durability of Positrodes for Protonic Ceramic Cells by Surface Decoration Via Infiltration. *J. Electrochem. Soc.* **2023,** *170*, 034506.
30. Kostogloudis, G. C.; Tsiniarakis, G.; Ftikos, C., Chemical Reactivity of Perovskite Oxide Sofc Cathodes and Yttria Stabilized Zirconia. *Solid State Ionics* **2000,** *135*, 529-535.
31. Kan, W. H.; Samson, A. J.; Thangadurai, V., Trends in Electrode Development for Next Generation Solid Oxide Fuel Cells. *Journal of Materials Chemistry A* **2016,** *4*, 17913-17932.
32. Jiang, S. P., A Review of Wet Impregnation—an Alternative Method for the Fabrication of High Performance and Nano-Structured Electrodes of Solid Oxide Fuel Cells. *Materials Science and Engineering: A* **2006,** *418*, 199-210.
33. Ding, D.; Li, X. X.; Lai, S. Y.; Gerdes, K.; Liu, M. L., Enhancing Sofc Cathode Performance by Surface Modification through Infiltration. *Energy & Environmental Science* **2014,** *7*, 552-575.
34. Shah, M.; Barnett, S. A., Solid Oxide Fuel Cell Cathodes by Infiltration of La0.6sr0.4co0.2fe0.8o3−Δ into Gd-Doped Ceria. *Solid State Ionics* **2008,** *179*, 2059-2064.
35. Shah, M.; Voorhees, P. W.; Barnett, S. A., Time-Dependent Performance Changes in Lscf-Infiltrated Sofc Cathodes: The Role of Nano-Particle Coarsening. *Solid State Ionics* **2011,** *187*, 64-67.
36. He, S.; Chen, K.; Saunders, M.; Quadir, Z.; Tao, S.; Irvine, J. T. S.; Cui, C. Q.; Jiang, S. P., Interface Formation and Mn Segregation of Directly Assembled La0.8sr0.2mno3 Cathode on Y2o3-Zro2 and Gd2o3-Ceo2 Electrolytes of Solid Oxide Fuel Cells. *Solid State Ionics* **2018,** *325*, 176-188.
37. He, S.; Chen, K. F.; Saunders, M.; Li, J.; Cui, C. Q.; Jiang, S. P., A Fib-Stem Study of La0.8sr0.2mno3 Cathode and Y2o3-Zro2/Gd2o3-Ceo2 Electrolyte Interfaces of Solid Oxide Fuel Cells. *J. Electrochem. Soc.* **2017,** *164*, F1437-F1447.
38. Sun, Y.; He, S.; Saunders, M.; Chen, K.; Shao, Z.; Jiang, S. P., A Comparative Study of Surface Segregation and Interface of La0·6sr0·4co0·2fe0·8o3-Δ Electrode on Gdc and Ysz Electrolytes of Solid Oxide Fuel Cells. *Int. J. Hydrog. Energy* **2021,** *46*, 2606-2616.
39. Jiang, S. P., Thermally and Electrochemically Induced Electrode/Electrolyte Interfaces in Solid Oxide Fuel Cells: An Afm and Eis Study. *J. Electrochem. Soc.* **2015,** *162*, F1119-F1128.
40. He, S.; Saunders, M.; Chen, K. F.; Gao, H. F.; Suvorova, A.; Rickard, W. D. A.; Quadir, Z.; Cui, C. Q.; Jiang, S. P., A Fib-Stem Study of Strontium Segregation and Interface Formation of Directly Assembled La0.6sr0.4co0.2fe0.8o3.Delta Cathode on Y2o3-Zro2 Electrolyte of Solid Oxide Fuel Cells. *J. Electrochem. Soc.* **2018,** *165*, F417-F429.
41. Ai, N.; Li, N.; He, S.; Cheng, Y.; Saunders, M.; Chen, K.; Zhang, T.; Jiang, S. P., Highly Active and Stable Er0.4bi1.6o3 Decorated La0.76sr0.19mno3+Δ Nanostructured Oxygen Electrodes for Reversible Solid Oxide Cells. *Journal of Materials Chemistry A* **2017,** *5*, 12149-12157.
42. He, S.; Jiang, S. P., Electrode/Electrolyte Interface and Interface Reactions of Solid Oxide Cells: Recent Development and Advances. *Progress in Natural Science-Materials International* **2021,** *31*, 341-372.
43. Yue, Z. W.; Jiang, L. Z.; Chen, Z. Y.; Ai, N.; Zou, Y. F.; Jiang, S. P.; Guan, C. Z.; Wang, X.; Shao, Y. Q.; Fang, H. H.; Luo, Y.; Chen, K. F., Ultrafine, Dual-Phase, Cation-Deficient Prba0.8ca0.2co2o5+? Air Electrode for Efficient Solid Oxide Cells. *Acs Applied Materials & Interfaces* **2023,** *15*, 8138-8148.
44. Chen, Z. Y.; Jiang, L. Z.; He, S.; Guan, C. Z.; Zou, Y. F.; Yue, Z. W.; Ai, N.; Jiang, S. P.; Shao, Y. Q.; Chen, K. F., Development of Intertwined Nanostructured Multi-Phase Air Electrodes for Efficient and Durable Reversible Solid Oxide Cells. *Appl. Catal. B-Environ.* **2022,** *305*, 121056.
45. Mai, A.; Becker, M.; Assenmacher, W.; Tietz, F.; Hathiramani, D.; Iverstiffee, E.; Stover, D.; Mader, W., Time-Dependent Performance of Mixed-Conducting Sofc Cathodes. *Solid State Ionics* **2006,** *177*, 1965-1968.

46. Chen, K. F.; Li, N.; Ai, N.; Cheng, Y.; Rickard, W. D. A.; Jiang, S. P., Polarization-Induced Interface and Sr Segregation of in Situ Assembled La0.6sr0.4co0.2fe0.8o3-Delta Electrodes on Y2o3-Zro2 Electrolyte of Solid Oxide Fuel Cells. *ACS Applied Materials & Interfaces* **2016,** *8*, 31729-31737.
47. Chen, K. F.; Li, N.; Ai, N.; Li, M.; Cheng, Y.; Rickard, W. D. A.; Li, J.; Jiang, S. P., Direct Application of Cobaltite-Based Perovskite Cathodes on the Yttria-Stabilized Zirconia Electrolyte for Intermediate Temperature Solid Oxide Fuel Cells. *Journal of Materials Chemistry A* **2016,** *4*, 17678-17685.
48. Esquirol, A.; Brandon, N. P.; Kilner, J. A.; Mogensen, M., Electrochemical Characterization of La0.6sr0.4co0.2fe0.8o3 Cathodes for Intermediate-Temperature Sofcs. *J. Electrochem. Soc.* **2004,** *151*, A1847-A1855.
49. Chen, K.; Ai, N.; Jiang, S. P., Origin of Low Frequency Inductive Impedance Loops of O2 Reduction Reaction of Solid Oxide Fuel Cells. *Solid State Ionics* **2016,** *291*, 33-41.
50. Chen, J.; Liang, F.; Liu, L.; Jiang, S.; Chi, B.; Pu, J.; Li, J., Nano-Structured (La, Sr)(Co, Fe)O3+Ysz Composite Cathodes for Intermediate Temperature Solid Oxide Fuel Cells. *Journal of Power Sources* **2008,** *183*, 586-589.
51. Chen, J.; Liang, F. L.; Chi, B.; Pu, J.; Jiang, S. P.; Jian, L., Palladium and Ceria Infiltrated La0.8sr0.2co0.5fe0.5o3-Delta Cathodes of Solid Oxide Fuel Cells. *J. Power Sources* **2009,** *194*, 275-280.
52. Bae, J. M.; Steele, B. C. H., Properties of La0.6sr0.4co0.2fe0.8o3-Delta (Lscf) Double Layer Cathodes on Gadolinium-Doped Cerium Oxide (Cgo) Electrolytes - I. Role of Sio2. *Solid State Ionics* **1998,** *106*, 247-253.
53. He, S.; Zhang, Q.; Maurizio, G.; Catellani, L.; Chen, K. F.; Chang, Q. B.; Santarelli, M.; Jiang, S. P., In Situ Formation of Er0.4bi1.6o3 Protective Layer at Cobaltite Cathode/Y2o3-Zro2 Electrolyte Interface under Solid Oxide Fuel Cell Operation Conditions. *Acs Applied Materials & Interfaces* **2018,** *10*, 40549-40559.

Table of Content